Journal of the European Ceramic Society 45 (2025) 117025

Contents lists available at ScienceDirect

Journal of the European Ceramic Society

journal homepage: www.elsevier.com/locate/jeurceramsoc

Ultrafast high-temperature sintering of aluminum nitride

Minwook Kim [a,1], Unseo Kim [a,1], Seon-Gyu Kim [b], Yunsang Kwak [b], Sung-Soo Ryu [c], Jaehun Cho [a,*]

[a] School of Materials Science and Engineering, Kumoh National Institute of Technology, Gumi, Gyeongbuk 39177, Republic of Korea
[b] Department of Mechanical System Engineering, Kumoh National Institute of Technology, Gumi, Gyeongbuk 39177, Republic of Korea
[c] Engineering Ceramic Center, Korea Institute of Ceramic Engineering and Technology, Icheon 17303, South Korea

ARTICLE INFO

Keywords:
Ultrafast high-temperature sintering
Aluminum nitride
Densification
Microstructure
Mechanical properties

ABSTRACT

Ultrafast high-temperature sintering (UHS) has received significant attention due to its effectiveness in consolidating ceramics in a very rapid manner. However, the application of UHS to non-oxide materials has been limited due to their extremely low sinterability. In this study, the UHS technique was applied to AlN to demonstrate its applicability and examine the resulting microstructure evolution and mechanical properties. High densification was achieved using electric currents of 47 A, 50 A, and 53 A for 240 s, with corresponding specimen temperatures of 1807.5 °C, 1872.8 °C, and 1935.6 °C. Vickers hardness increases up to 240 s but decreases at 300 s due to grain growth and sublimation of secondary phases. Fracture toughness decreases with larger grain sizes showing the inverse relationship between grain size and toughness. This study demonstrates that UHS is applicable to non-oxide ceramics, which offers significant potential for energy savings and rapid processing in non-oxide ceramic manufacturing.

1. Introduction

Aluminum nitride (AlN) has emerged as a significant material in the field of advanced ceramics owing to its remarkable thermal and electrical properties. The unique combination of high thermal conductivity, excellent thermal shock resistance, low thermal expansion coefficient, strong electrical insulation, and chemical stability makes AlN an ideal candidate for heat dissipation substrates in power modules and electronic devices particularly in the rapidly growing sector of electric vehicles [1–6]. However, achieving high densification in AlN ceramics presents substantial challenges attributed to its strong covalent bonds due to which achieving full densification requires sintering temperatures above 1950 °C [4,7]. These high sintering temperatures not only lead to rapid grain growth, which can deteriorate the mechanical properties of the material [8], but also result in high energy consumption and increased production costs.

To address the challenges associated with the poor sinterability of AlN, sintering additives are commonly used to promote densification at lower temperatures through liquid phase sintering. Among these additives, Y_2O_3 stands out as one of the most effective sintering aids [9,10]. It reacts with the Al_2O_3 layer residing on the surface of AlN particles, which eventually forms liquid yttrium aluminate secondary phases such as $Y_3Al_5O_{12}$ (yttrium aluminum garnet, YAG), $Y_4Al_2O_9$ (yttrium aluminum monoclinic, YAM), and $YAlO_3$ (yttrium aluminum perovskite, YAP), when the temperature exceeds their eutectic point [11]. Additionally, Y_2O_3 acts as a scavenger by removing oxygen impurities from the AlN lattice, which enhances the thermal conductivity of AlN ceramics [12–14]. Typically, adding 3–5 wt% Y_2O_3 is found to be most effective for this purpose [15]. However, incorporating more than 5 wt% Y_2O_3 can reduce the thermal conductivity of AlN by forming excessive low-conductivity Al_2O_3-Y_2O_3 secondary phases [15].

Another approach to achieving high-density AlN at relatively lower temperatures includes incorporating additional modules into the furnace that apply external pressure and/or electric currents, such as hot pressing [16], hot isostatic pressing [17], high gas pressure combustion [18], and spark plasma sintering [19]. However, these techniques typically require several hours of processing time, which still limits the potential to fully minimize energy consumption. In contrast, recently developed ultrafast high-temperature sintering (UHS) has emerged as a revolutionary method with significant potential for industrial applications [20]. The UHS technique utilizes Joule heating generated by a strong current flowing through electrically conductive materials, such as

* Corresponding author.
E-mail address: jhcho@kumoh.ac.kr (J. Cho).
[1] These authors contributed equally to this work.

https://doi.org/10.1016/j.jeurceramsoc.2024.117025
Received 17 July 2024; Received in revised form 8 October 2024; Accepted 25 October 2024
Available online 28 October 2024

graphite. The extremely high heating rates ranging from 10^4 to 10^5 °C/min can rapidly heat up a green body inserted inside the conductive materials and thus result in a high degree of densification within a few mins [21]. The short processing time not only significantly reduces energy consumption but also prevents excessive grain growth, which makes UHS a strong candidate for a highly efficient and effective sintering method for AlN ceramics.

The application of the UHS technique for oxide-based materials has been extensively studied [22–35], but research on non-oxide systems remains limited to SiC [36], Si_3N_4 [37], ZrC [38], and ZrB_2 [39]. In this study, we demonstrate the applicability of the UHS technique for AlN for the first time. Our objective is to achieve high-density AlN in a short duration while conserving energy and eliminating the need for external pressure. The microstructure evolution and mechanical properties of AlN prepared by the UHS technique are investigated and shown to be comparable to those prepared by the conventional way. This study highlights that the UHS technique is a viable and cost-effective alternative to traditional sintering methods for densifying AlN, which may pave the way for advancements in various high-performance ceramic applications.

2. Materials and methods

The aluminum nitride (AlN) powder used in this study has a primary particle diameter of 0.6 μm (H-grade, Tokuyama, Tokyo, Japan). The sintering additive of Y_2O_3 with a particle size of 50 nm and a specific surface area of 30–50 m^2/g was employed (Sigma-Aldrich, St. Louis, USA). The powder composition was fixed at 95 wt% AlN and 5 wt% Y_2O_3 and thoroughly mixed using a ball milling process. The mixed powders were milled at 155 rpm for 24 h using 3 mm zirconia balls and ethanol milling media, with a weight ratio of 1:1:5 for powders, ethanol, and balls. After milling, the slurry was dried in a vacuum oven at 80 °C for 12 h. The dried powders were then filtered through a 200 μm mesh sieve to obtain fine powders. After powder processing, 0.8 g of the mixture powder was placed into a cylindrical mold with a diameter of 15 mm and uniaxially pressed for 40 s with 80 MPa to form a disc-shaped pellet. Subsequently, the pellets are subjected to cold isostatic pressing, which uses ethylene glycol as a compression fluid to apply 200 MPa pressure for 5 min to ensure that all parts of the pellet have a uniform density.

For densification of AlN green body through the UHS technique, all tests were carried out in a glove box filled with Ar. Graphite felt was used as a heating material with a dimension of 100 mm in length, 30 mm in width, and 11.5 mm in thickness. The green body was positioned centrally inside the graphite felt while two brass electrodes clamped the felt with a distance of 30 mm between the electrodes. A direct current power supply (TS1560A, Toyotech Co., Ltd. Incheon, Republic of Korea) was employed to apply electric currents. The variable parameters chosen for this study were electric currents of 47, 50, and 53 A with durations of 30, 60, 120, 180, 240, and 300 s. The current ramping rate was set to be 5 A/s with the cooling rate being the same. For comparison, a conventional AlN ceramic with 5 wt% Y_2O_3 additive was prepared using pressureless sintering in a graphite furnace under a nitrogen atmosphere. It was sintered at 1800 °C for 120 min with a heating rate of 10 °C/min to 1200 °C, followed by a 20-min hold at 1200 °C to switch thermocouple to pyrometer for high temperature measurement. The heating rate was then reduced to 5 °C/min up to 1800 °C. The temperature profile of the conventional sintering process is illustrated in Figure S1. The conventional sintering process without cooling took approximately 6 hr. It took more than 12 hr including cooling process. The density of the conventionally sintered sample was measured using Archimedes' principle, yielding a relative density of 91 %.

Numerical analysis was conducted using the finite element method (FEM) to observe the temperature changes throughout the entire system. The commercially available advanced numerical software, COMSOL Multiphysics, was employed for the temperature evaluation. The electromagnetic heating and heat transfer with surface-to-surface radiation modules were utilized to replicate the experiments more accurately. The UHS model was developed by applying the electric current using a terminal function. Specifically, one end face of the brass electrode in contact with the graphite felt was assigned as the terminal (positive terminal) and the opposite brass electrode as the ground (negative terminal). This setup as shown in Figure S2 accurately represents the actual experimental conditions, where current flows from one electrode to the other through the graphite felt and the sample. The change in electrical conductivity with varying temperatures was also considered. Additionally, the impedance of each system was incorporated into the model to apply the correct current values. The impedance was calculated using the voltages measured during the actual experiments, which were 10.8 V, 11.4 V, and 12 V for the currents of 47 A, 50 A, and 53 A, respectively. By considering both the current and voltage, it was ensured that the power input and electrical behavior in the simulations closely matched the experimental conditions.

After the UHS process, the densities of all sintered bodies were measured by geometrical density for porous specimens, and the Archimedes method for sufficiently densified samples. For microstructural characterization, the sintered body was polished uniformly to remove irregularities and surface impurities from graphite felt. Initially, the specimens were ground using a rotating polishing wheel (FOBOS-200F, MTDI, Daejeon, Republic of Korea) with 600, 1200, and 2000 grit sandpapers. Subsequently, fine polishing was performed using 6, 3, and 1 μm diamond pastes, followed by 0.06 μm colloidal silica. In addition, ultrasonic cleaning was performed three times for 10 min each in ethanol at the end of each fine polishing stage. After polishing, XRD, SEM, and EDS analyses on the UHS samples showed no evidence of carbon contamination within the samples. A solution of 0.5 N nitric acid and 0.8 N phosphoric acid mixed at a volume ratio of 1:2 was used as an etchant. The specimens were immersed in the etchant for 2 min for chemical etching and subsequently subjected to thermal etching at 1100 °C for 10 min in a nitrogen environment.

X-ray diffraction (XRD) analysis (SmartLab, Rigaku, Tokyo, Japan) was employed to examine the crystal structure and formation of secondary phases in the sintered body. The microstructure of the polished samples was investigated using a field emission scanning electron microscope (FE-SEM, MAIA III, Tescan, Brno, Czech Republic) operating at a voltage of 10 kV. Chemical analysis was conducted using energy dispersive x-ray spectroscopy (EDS) integrated into the SEM. The average grain size was measured for more than 100 grains using the Equivalent Circle Diameter (ECD) method based on the obtained SEM images.

For mechanical property measurements such as elastic modulus and Vickers hardness, more than 20 indentations were performed on each specimen using a micro combi tester (MCT^3, Anton Paar GmbH, Graz, Austria) with a load of 100 mN. The fracture toughness was measured using the length of the cracks that form at the corners after indentation. For fracture toughness, only specimens with a relative density higher than 97 % were tested, as it is difficult to observe cracks in specimens with low relative density due to the presence of high-density pores.

3. Results and discussion

Fig. 1a-c show the SEM images of raw AlN powder, Y_2O_3 powders, and mixed powders after the ball milling process, respectively, captured using a secondary electron detector. The images reveal the submicron particle size and spherical shape of AlN particles, along with the nano-sized Y_2O_3 particles. The XRD patterns of the starting materials and mixed powder are illustrated in Fig. 1d. The sharp peaks corresponding to the hexagonal AlN phase and cubic Y_2O_3 phase are observed (represented in blue and red, respectively), while the mixed powder is represented in black. Fig. 1e illustrates the current profile of the UHS process where electric currents of 47 A, 50 A, and 53 A were applied with a ramping rate of 5 A/s and holding time of 30, 60, 120, 180, 240, and 300 s. The schematic diagram of the UHS sintering setup is as shown in

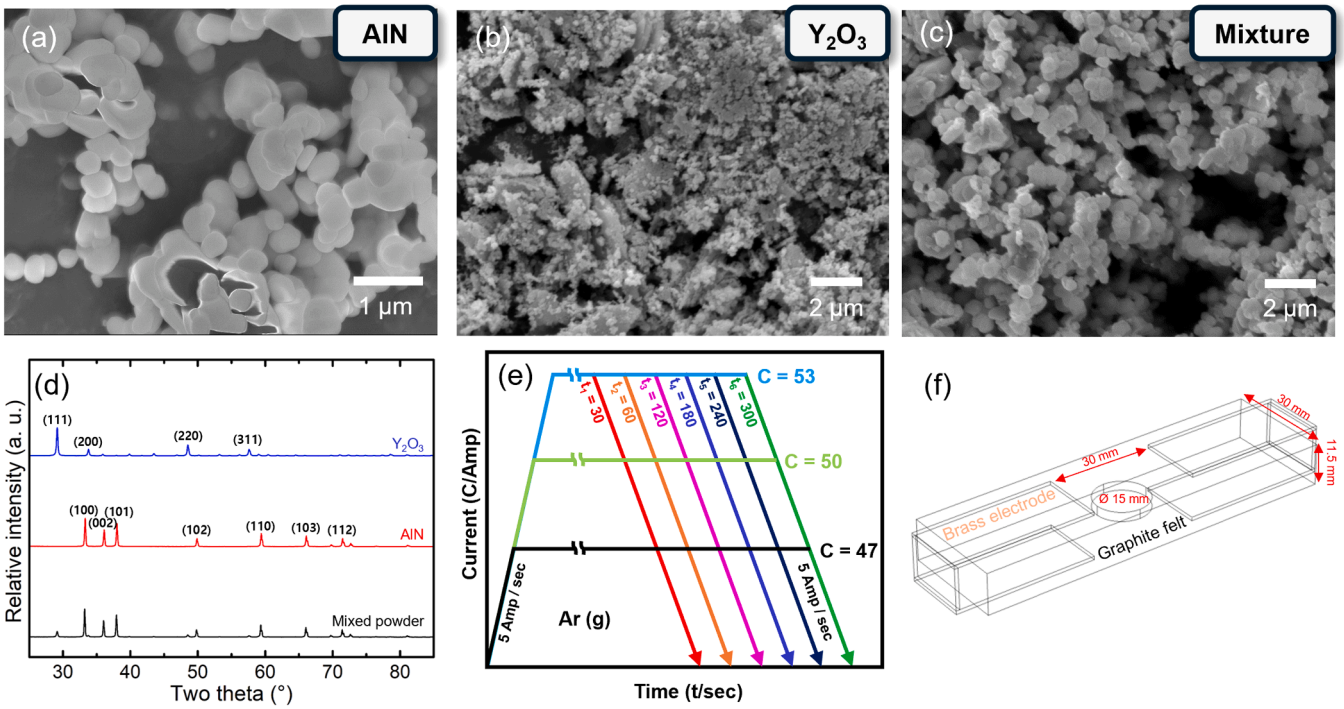

Fig. 1. (a) SEM micrograph of raw AlN powder revealing a primary particle size of 0.6 μm and spherical shape. (b) SEM micrograph of nanosized Y_2O_3 powder. (c) SEM micrograph of the mixed powder after ball milling for 24 h followed by drying process. (d) XRD patterns of as-received AlN, Y_2O_3, and the mixed powder showing sharp peaks for cubic Y_2O_3 (blue), hexagonal AlN (red), and the mixed powder (black). (e) Electric current profile of the UHS process with currents of 47 A, 50 A, and 53 A applied for various holding times of 30, 60, 120, 180, 240, 300 s. (f) Schematic of the UHS process illustrating the green body located at the center of the graphite felt with a distance of 30 mm between the brass electrodes.

Fig. 1f. The green body with a diameter of 15 mm was positioned at the center of the graphite felt after creating a slit to accommodate it. Brass electrodes were used, and the distance between the electrodes was consistently set to 30 mm throughout all experiments, which were performed in an Ar atmosphere to prevent oxidation of the graphite, AlN, and electrodes.

For accurate temperature evaluation using FEM, it is essential to use the adequate electric and thermal properties of AlN. These values were selected based on established data from the literature to ensure the accuracy of the simulations [40–43]. AlN exhibits a negative temperature coefficient meaning that its electrical conductivity increases as the temperature rises. To account for this behavior, a temperature-dependent conductivity equation was applied in this study, as detailed in Table 1 [15]. In addition to electrical conductivity, other critical properties of AlN were considered. The relative permittivity was set at 9.2, while the heat capacity at constant pressure was 740 $J{\cdot}kg^{-1}{\cdot}K^{-1}$ [40,43]. The density and surface emissivity were taken as 3260 kg/m^3 and 0.5, respectively [41,42]. Thermal conductivity typically decreases dramatically with increasing temperature. This inverse relationship is crucial for modeling purposes, as it affects heat dissipation and temperature distribution within the material significantly. By extrapolating experimental data from a previous study, a temperature-dependent equation for the thermal conductivity of AlN was derived and incorporated into the FEM simulations, as shown in Table 1 [15]. The electric and thermal properties of the graphite felt and brass are also present in Table 1.

Fig. 2a presents a thermal simulation image under the sintering conditions of 53 A for 300 s illustrating the heat distribution of the graphite felt, the brass electrodes, and the AlN specimen. The detailed temperature profiles calculated by FEM are shown in Fig. 2b-d corresponding to electric currents of 47 A, 50 A, and 53 A, respectively. In these graphs, the red curve represents the maximum temperature of the graphite felt, whereas the green and blue curves show the temperature

Table 1
Electric properties and thermal properties of AlN, graphite felt, and brass applied for FEM analysis [15,40–44].

Property	Units	AlN	Graphite felt	Brass
Electrical conductivity	S/m	$6.89 \times 10^3 \times \left(e^{-0.17/(8.617\times10^{-5}\times T_{AlN})}\right) \times 10^2$	$155.95 \times \ln(T_G) - 379.93$	5.998×10^7
Relative permittivity	-	9.2	18	1
Heat capacity at constant pressure	J/(kg·K)	740	$647.41 \times \ln(T_G) - 2780$	385
Density	Kg/m^3	3260	87	8940
Thermal conductivity	W/(m·K)	$38028 \times T_{AlN}{}^{-0.967}$	$6 \times 10^{-11} \times T_G^3 - 7 \times 10^{-8} \times T_G^2 + 10^{-4} \times T_G - 0.0175$	400
Surface emissivity	-	0.5	0.9	0.6

of the AlN specimen and the brass electrodes, respectively. The FEM simulations estimated the steady-state temperatures of the AlN specimens to be 1807.5 °C for 47 A, 1872.8 °C for 50 A, and 1935.6 °C for 53 A. These temperatures are sufficiently high to achieve effective densification of AlN with a sintering aid of Y_2O_3 [6]. Despite the absence of external pressure and very short duration of sintering process, the ultrafast heating rates achieved through the UHS technique are crucial in facilitating the densification behavior of AlN by maintaining the submicron-sized AlN particles at high temperatures. This preservation of

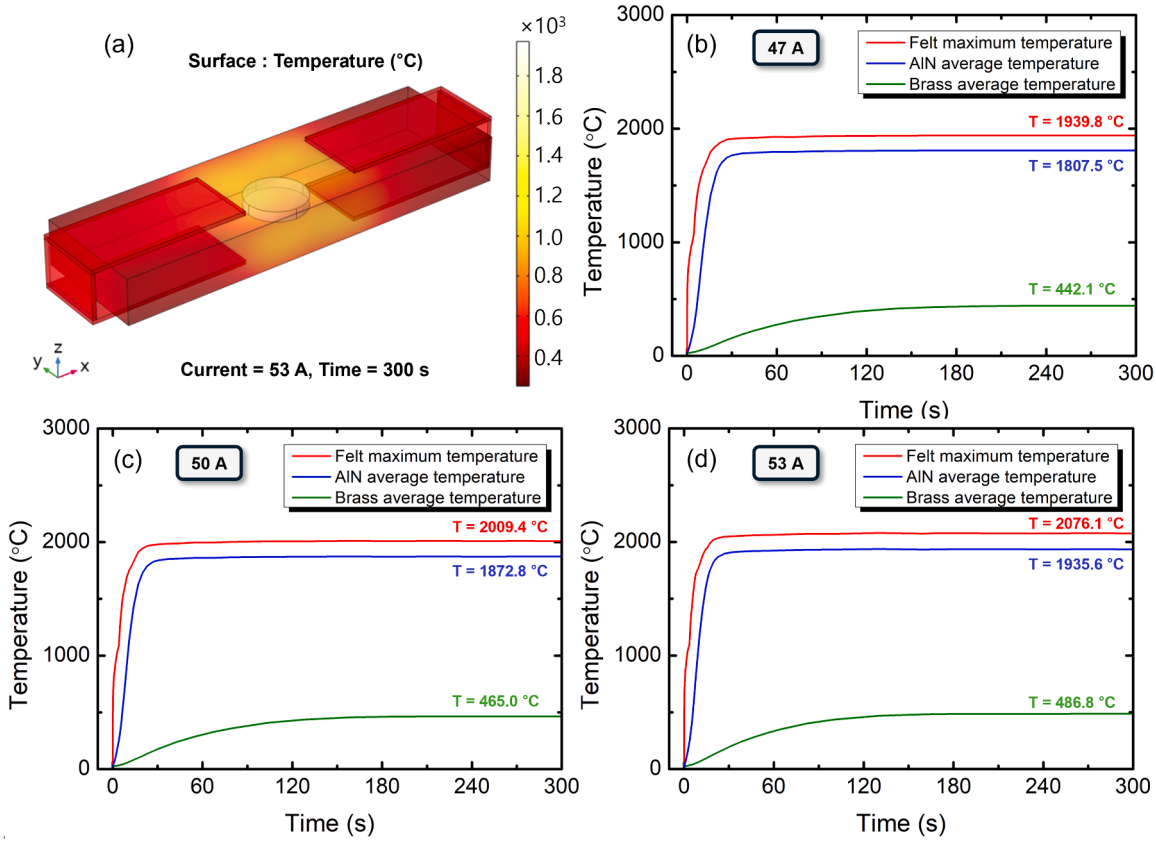

Fig. 2. (a) Thermal simulation image under sintering conditions of 53 A for 300 s. Temperature profiles calculated by the FEM for electric currents of (b) 47 A with a steady-state temperature of the AlN specimen at 1807.5 °C, (c) 50 A with a steady-state temperature of the AlN specimen at 1872.8 °C, and (d) 53 A with a steady-state temperature of the AlN specimen at 1935.6 °C.

particle size sustains the driving force for densification at elevated temperatures, which ensures that the high degree of densification can be achieved without significant grain growth [45]. On the other hand, the temperatures of the two brass electrodes are calculated to be 442.1, 465.0, and 486.8 °C for currents of 47, 50, and 53 A, respectively. These temperatures are well below the melting point of the brass (930 °C). This observation aligns with our experimental results where no deformation or melting of the electrodes was observed.

The temperature gradients between the graphite felt and the sample are around 130 ~ 140 °C, which is reasonable given the thermal properties and dimensions of the materials involved. It is observed in the simulations that the temperature difference between the graphite felt and the AlN sample stabilizes and remains nearly constant once steady-state conditions are reached. This occurs because the system reaches a thermal equilibrium that includes not only the graphite felt and the sample but also the surrounding environment (Ar atmosphere). All three modes of heat transfer were considered in the model, which are conduction (heat transfer between the graphite, the sample, and the brass electrodes), convection (heat loss to the surrounding Ar atmosphere), and radiation (thermal radiation emitted from the surfaces of the graphite felt, the sample, and the brass to the surroundings). The AlN sample with much lower electrical and thermal conductivity compared to graphite felt absorbs heat primarily through conduction from the surrounding graphite felt. However, both the graphite felt and the sample lose heat to the environment through convection and radiation. The temperature difference between the graphite felt and the sample remains relatively constant of 130 ~ 140 °C over time because the rate of heat transfer from the graphite felt to the sample is balanced by the heat losses from both the graphite felt and the sample to the surroundings. The system reaches a dynamic equilibrium where the temperatures stabilize, and the heat input, heat transfer within the materials, and heat losses are balanced.

Fig. 3a shows the relative density of each specimen sintered at different currents and holding times. For the first 60 s, little increase in relative density is observed for all currents. This can be attributed to the poor thermal conduction of the AlN green bodies, which is due to the gaps between particles before neck formation occurs. However, at 120 s, a significant increase in densification is observed, with higher electric fields resulting in higher densification rates. For instance, applying 53 A results in a relative density of 90 % after 120 s. After 240 s of current application, all specimens reached over 95 % relative density, which indicates near-complete densification. This high densification level suggests that the UHS technique can effectively overcome the intrinsic poor sinterability of AlN only within a few mins. The extremely rapid heating rate of this technique (10^4 to 10^5 °C/min) minimizes the exposure of AlN particles to intermediate temperatures where significant grain growth typically occurs. As a result, very fine grains are preserved even at high temperatures during densification [45]. In high-temperature regimes, the process promotes densification rather than grain coarsening.

Interestingly, a decrease in relative density is observed for the specimen sintered at 53 A for 300 s. YAG phase in the AlN matrix can sublimate at temperatures above 1850 °C, and YAP also sublimates below 1850 °C [46]. The estimated sample temperature under 53 A is 1935.6 °C, which is sufficiently high to induce the sublimation of these secondary phases. The sublimation of these phases can lead to the formation of voids and loss of mass without changing apparent volumes, and thus reduces the overall density. Therefore, the observed decrease in density for the specimen sintered at 53 A for 300 s is likely due to the loss of secondary phases caused by extremely high temperatures. Fig. 3b-d present the XRD patterns of each specimen sintered under different currents for various durations. Dominant peaks of hexagonal

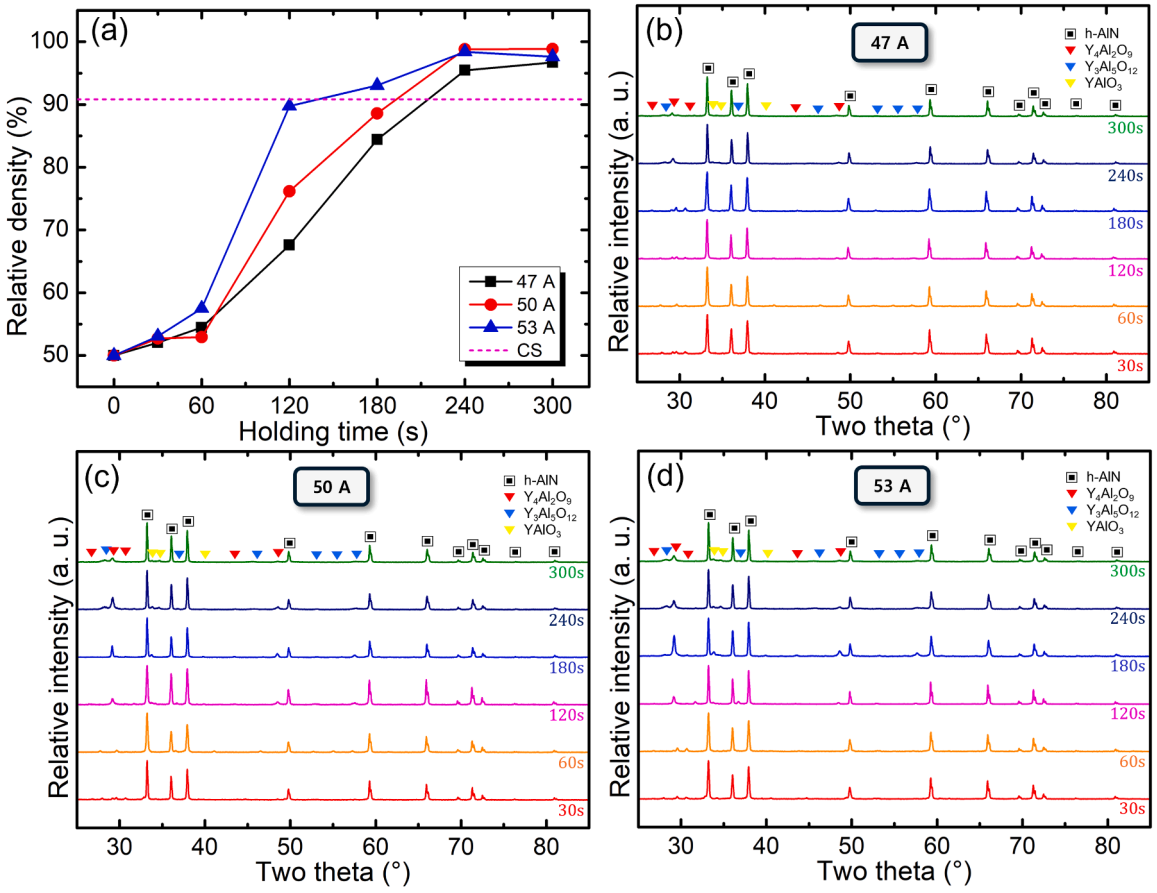

Fig. 3. (a) Relative densities of each specimen sintered under different electric currents for various holding times. CS stands for the conventionally sintered AlN. XRD patterns of specimens with applied currents of (b) 47 A, (c) 50 A, and (d) 53 A. The peaks of the secondary phases vary depending on the holding time and input current.

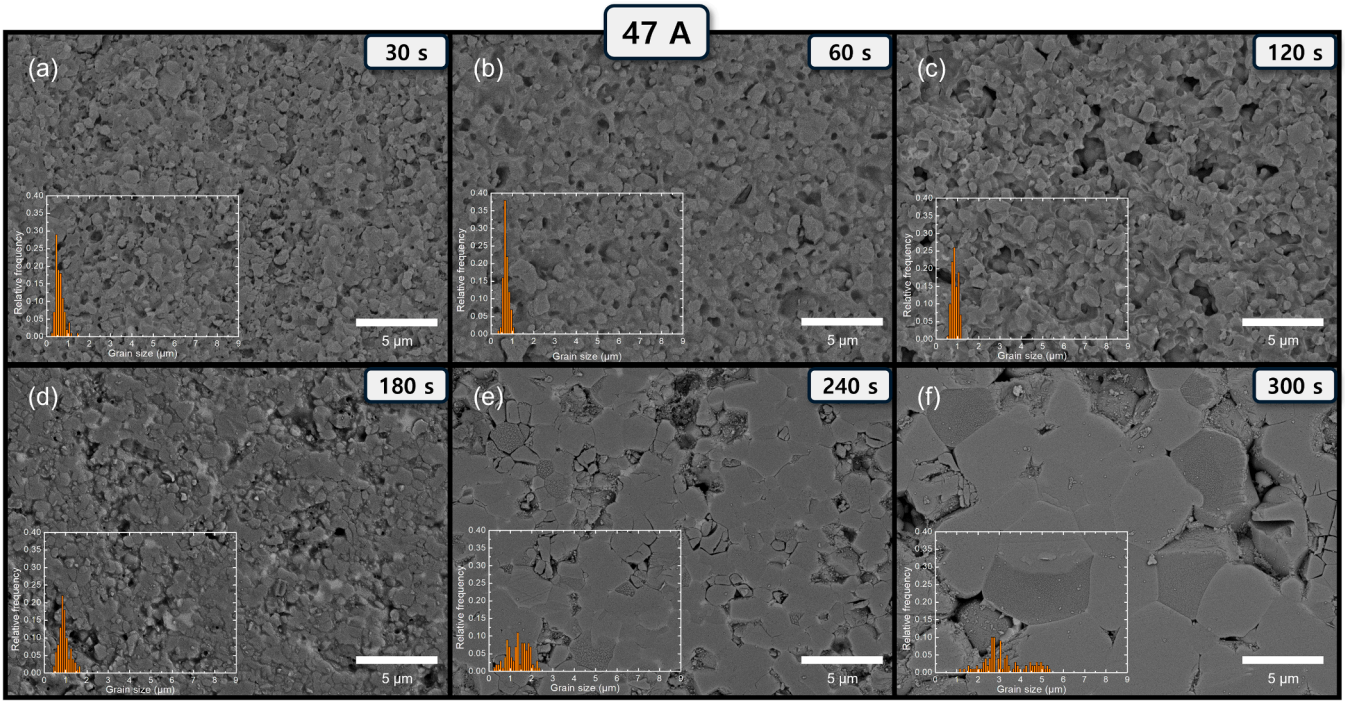

Fig. 4. SEM micrographs showing the microstructure of the sintered bodies under applied electric current of 47 A at different holding time of (a) 30 s, (b) 60 s, (c) 120 s, (d) 180 s, (e) 240 s, and (f) 300 s. All images were taken at the same magnification. The grain size distribution for each specimen is included in the inset.

AlN are observed along with minor peaks from secondary phases including YAG, YAM, and YAP. The relative intensity of these secondary phases in the XRD patterns tends to increase up to a sintering duration of 180 s and then decreases. Again, it is believed that this decrease can be attributed to the sublimation of secondary phases at high temperatures.

To explore alternative explanations for the reduced relative density such as lattice expansion due to the diffusion of Y into the AlN lattice, the real crystallographic density of the samples sintered at 53 A for various holding times was calculated using the lattice parameters obtained from XRD data as shown in Figure S3. The XRD data show that prolonged holding times did not lead to lattice expansion, suggesting that Y did not significantly diffuse into the AlN lattice. This observation is consistent with the extremely low solubility of Y in the AlN lattice, given the significant different in ionic radii between Y^{3+} (0.90 Å) and Al^{3+} (53 Å). Therefore, the decrease in density is unlikely to be due to lattice expansion caused by Y diffusion.

Interestingly, it was observed that the crystallographic densities of the samples were slightly higher than the theoretical value of 3.26 g/cm^3 for AlN. It is hypothesized that this could be due to the formation of aluminum vacancies. When Al_2O_3 on the surface of AlN particles reacts with Y_2O_3, it can leave negatively charged aluminum vacancies and positively charged oxygen ions occupying nitrogen sites as following [47].

$$Al_2O_3 \rightarrow 2Al_{Al}^{x} + 3O_N^{\bullet} + V_{Al}^{'''}$$

These defects can distort the lattice, leading to slight reduction in lattice volume and affecting the crystallographic density.

Fig. 4 shows the SEM images of the polished surfaces for specimens sintered under an electric current of 47 A for 30, 60, 120, 180, 240, and 300 s, all captured at the same magnification. Inset figures show the grain size distribution at the same scale, calculated using the ECD method. For the specimen sintered for 30 s, individual particles are clearly visible with no significant densification. At this stage, the particles are separated from one another. When the sintering duration is extended to 60 and 120 s, the formation of necks between particles becomes evident, while grain growth remains limited. This neck formation indicates the transition to the intermediate stage of sintering only within the first 2 mins. At 180 s, significant densification is observed with the microstructures showing a more continuous network of grains with fewer and smaller pores. For specimens sintered for 240 s and 300 s, severe grain growth is observed combined with isolated pores near the triple junctions. This can be attributed to the entrapment of Ar gas and the coarsening of grains which reduces the driving force for pore elimination [48]. Additionally, as the sintering duration increases, the grain size distribution becomes less sharp, shifts towards larger sizes, and broadens overall. When the specimens were subjected to higher electric currents of 50 and 53 A, a consistent trend in microstructure evolution is observed as shown in Figs. 5 and 6, respectively.

Interestingly, for a specimen sintered under the conditions of 53 A for 300 s, triple junctions become more prominent and exhibit larger pores, compared to the counterparts sintered under 47 and 50 A for 300 s. Backscattered electron SEM images for the specimen sintered at 53 A for 300 s in Fig. 7 confirms the presence of pores at and near the triple junctions, which were initially filled with secondary phases. The sublimation of these phases due to excessive heat likely left behind these pores, which eventually contributes to the decrease in density [46]. In addition, the weight loss data shown in Fig. 7 indicate that higher currents and longer holding times lead to significant weight loss, with over 10 % weight loss observed for the specimen sintered at 53 A for 300 s. This substantial weight loss supports the idea that sublimation of secondary phases occurs under these conditions.

The average grain size of AlN measured with more than 100 grains through the ECD method is shown in Fig. 8. For specimens sintered under an electric current of 47 A, the average grain size remained below 1 μm until a sintering duration of 180 s. Beyond this point, a significant increase in grain size was observed, reaching 1.36 and 3.23 μm at sintering durations of 240 and 300 s, respectively. In the case of a 50 A current, the average grain size exceeded 1 μm after just 120 s of sintering. It continued to grow progressively to 1.15 μm at 180 s, and drastically to 2.69 μm at 240 s, and 3.89 μm at 300 s. Similarly, under a 53 A current, the average grain size surpassed 1 μm at 120 s. This increase continued with grain sizes reaching 1.31 μm at 180 s, 3.24 μm at

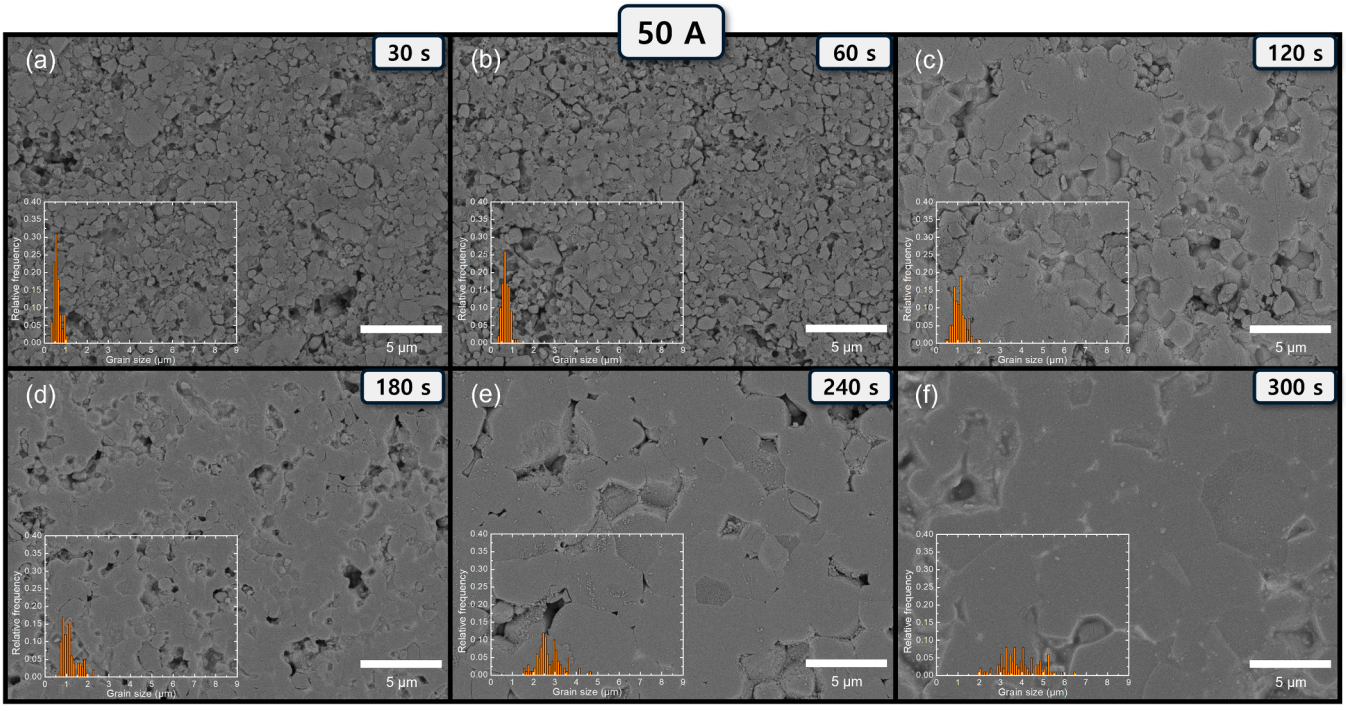

Fig. 5. SEM micrographs showing the microstructure of the sintered bodies under applied electric current of 50 A at different holding time of (a) 30 s, (b) 60 s, (c) 120 s, (d) 180 s, (e) 240 s, and (f) 300 s. All images were taken at the same magnification. The grain size distribution for each specimen is included in the inset.

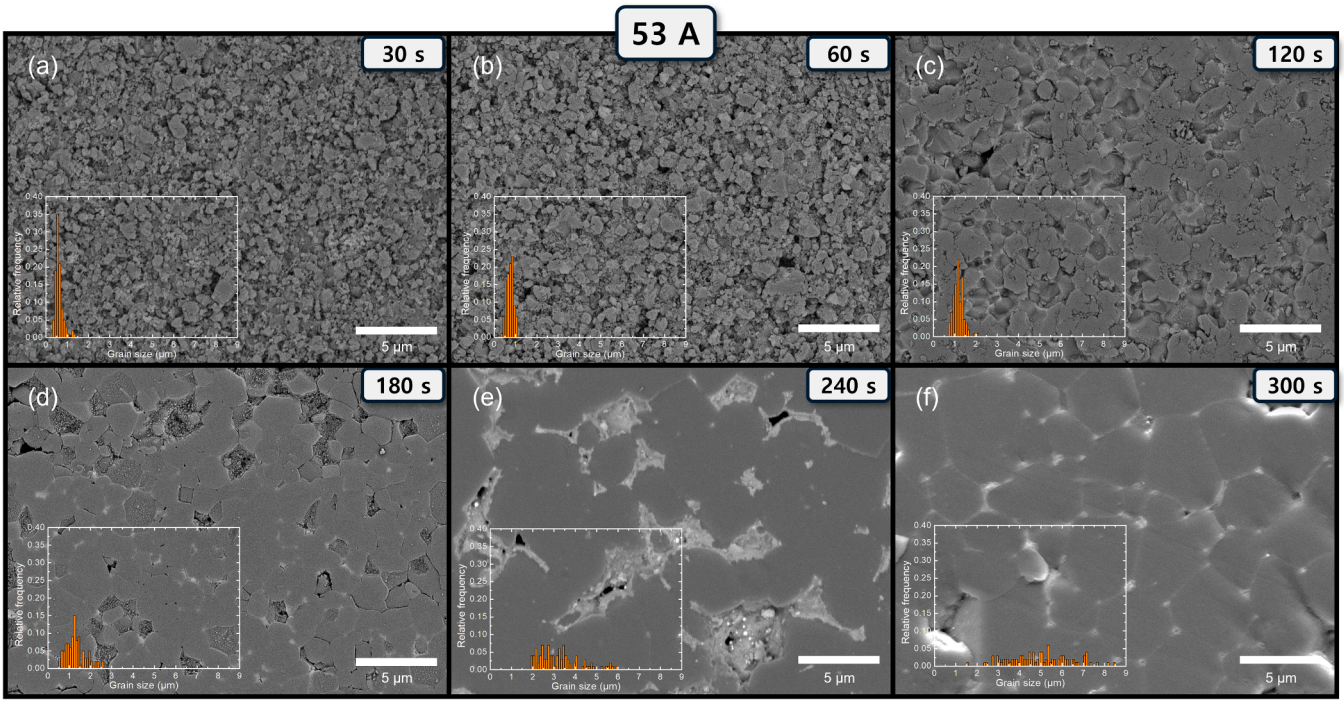

Fig. 6. SEM micrographs showing the microstructure of the sintered bodies under applied electric current of 53 A at different holding time of (a) 30 s, (b) 60 s, (c) 120 s, (d) 180 s, (e) 240 s, and (f) 300 s. All images were taken at the same magnification. The grain size distribution for each specimen is included in the inset.

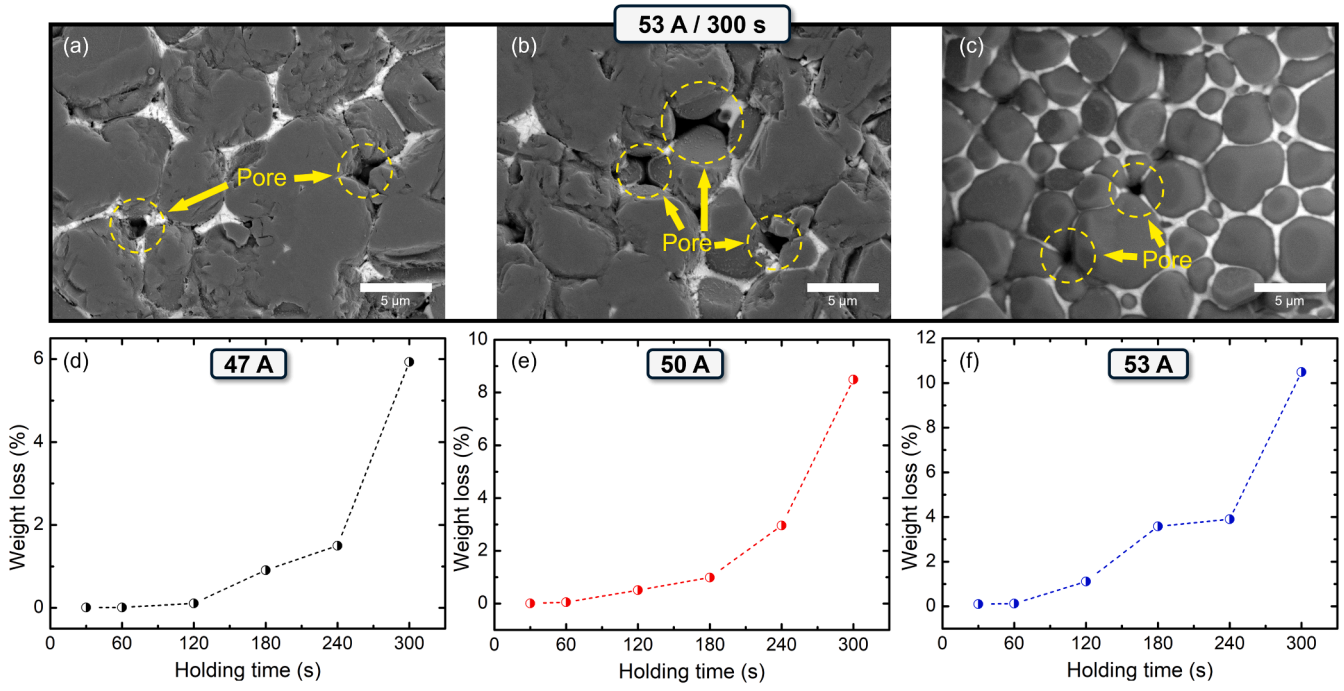

Fig. 7. (a-c) Backscattered electron SEM images of the sample sintered at 53 A for 300 s showing the presence of pores at triple junctions. (d-f) Weight loss percentages of each specimen sintered at 47, 50, and 53 A for different times.

240 s, and 4.94 μm at 300 s. In comparison, as shown in Figure S4, the SEM images of the conventionally sintered AlN ceramic show porous structure with insignificant grain growth despite its long process time at the maximum temperature of 1800 °C. The average grain size was calculated to be 1.2 μm from SEM images using the equivalent circle diameter method as shown in Figure S4d. This value is similar to that of UHS AlN ceramics prepared at 47 A for 4 min, 50 A for 3 min, and 53 A for 3 min.

The presence of secondary phases along grain boundaries for a specimen processed under 50 A for 300 s was confirmed by the SEM images with a back scattered electron detector as shown in Fig. 9. In the BSE image shown in Fig. 9a, the AlN grains are slightly darker than the secondary phases along grain boundaries. The secondary phases between grains consist of Y and O elements, and thus confirming the

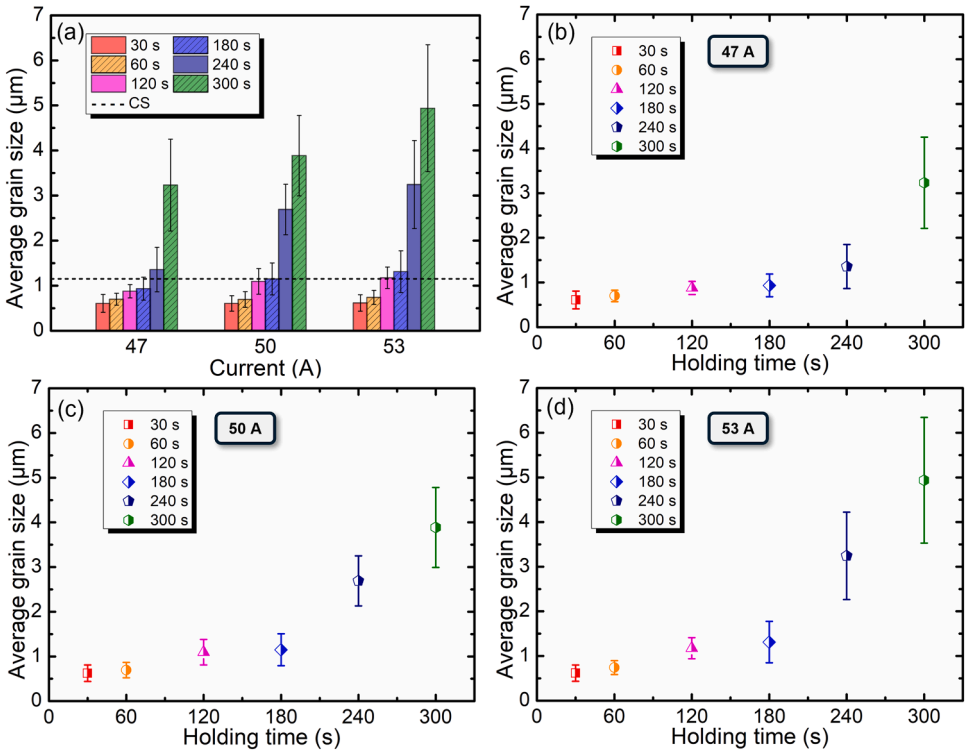

Fig. 8. (a) Average grain size of all specimens sintered under 47, 50, and 53 A for 30, 60, 120, 180, 240, and 300 s. CS stands for the conventionally sintered AlN. Average grain size of specimens processed under (b) 47 A, (c) 50 A, and (d) 53 A.

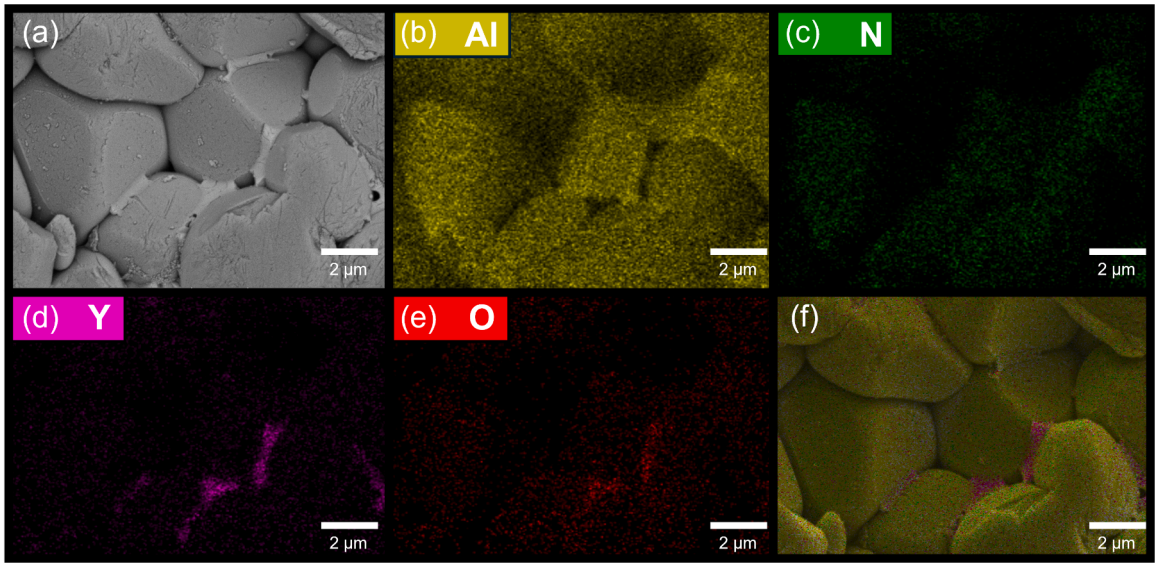

Fig. 9. (a) SEM micrograph of a specimen sintered under an electric current of 50 A for 300 s captured using the backscattered electron detector. The corresponding EDS images for individual elements including (b) Al, (c) N, (d) Y, and (e) O. (f) The EDS mapping showing the overlap of all detected elements.

formation of Al_2O_3-Y_2O_3 second phases including YAM, YAG, and YAP. The presence of this secondary phase suggests that the UHS technique induces sufficiently high temperatures for the Y_2O_3 sintering aid to react with Al_2O_3 despite a short period of time and facilitate densification through a liquid phase sintering. In addition, Figure S5 shows backscattered electron SEM image and EDS elemental map of the specimen processed at 53 A and 300 s. The average chemical compositions obtained from the secondary phases along grain boundaries were consistent with the theoretical stoichiometries of YAM, YAG, and YAP phases, as shown in Table S1-3. This suggests that the rapid heating and short sintering duration in the UHS technique do not adversely affect the formation or composition of the liquid phases necessary for effective liquid-phase sintering.

As evidenced by XRD, SEM, and EDS analyses, the dominant sintering mechanism during UHS of AlN ceramics with Y_2O_3 additive is liquid-phase sintering. The liquid phases wet the solid AlN grains, which eventually covers their surfaces and promoting mass transport. The AlN-Y_2O_3 system aims to minimize its total interfacial energy, which includes the solid-solid grain boundaries and the solid-liquid interfaces. A rounded or spherical grain shape (as observed in the microstructural

analyses shown in Fig. 7) is direct evidence that liquid-phase sintering is dominant. This morphology minimizes the surface area-to-volume ratio, thereby reducing the total interfacial energy.

The rounding of grains is facilitated by enhanced mass transport through solution-precipitation mechanisms, where AlN dissolves from regions of high curvature (edges and corners) and precipitates onto regions of lower curvature (flatter surfaces), which effectively smooths out the grains [49]. To verify the grain growth behavior and sintering mechanism, the grain growth kinetics were analyzed by plotting grain size versus relative density for the experiments conducted at 47, 50, and 53 A. The sintering trajectory in Figure S6 shows the competing effects of densification and coarsening during UHS. This plot presents a typical evolution of a sintering body, showing an almost flat trajectory up to relative densities of approximately 90 %, followed by a much steeper slope thereafter [50]. This trajectory is somewhat different from previous reports, such as the UHS of $Li_{6.5}La_3Zr_{1.5}Ta_{0.5}O_{12}$, where a linear correlation between grain size and relative density was observed, and rapid grain growth in the final stage was not reported [20]. The grain growth kinetics were further studied using the following equation:

$$d^n - d_0^n = Kt$$

where d is the average grain size at time t, d_0 is the initial grain size, n is the grain growth exponent, and K is a temperature-dependent rate constant. When the grain growth exponent n is 2, the rate-limiting step of grain growth is typically interface reaction-controlled, whereas when n is 3, it is diffusion-controlled [51]. The linear parts of the intermediate sintering stage for each current were taken to calculate K, which was used to estimate the activation energy of grain growth using the following equation:

$$K = k_0 \exp\left(\frac{E_a}{RT}\right)$$

where k_0 is a pre-exponent constant, E_a is an activation energy, R is the ideal gas constant, and T is the absolute temperature estimated by the FEM simulation. The experimental data fit better with $n = 3$, yielding a higher coefficient of determination ($R^2 = 0.9354$) as shown in Figure S6f. This suggests that grain growth during UHS of AlN is diffusion-controlled, specifically through a solution-reprecipitation process involving AlN diffusion in the liquid phase, which is consistent with other techniques such as microwave sintering and pressureless sintering [49,51]. The activation energy for grain growth was calculated to be 412.1 kJ/mol. In contrast, assuming $n = 2$ (reaction-controlled grain growth) resulted in a lower coefficient of determination ($R^2 = 0.9241$) and an activation energy of 331.9 kJ/mol (as shown in Figure S6d) indicating a less favorable fit. Therefore, the analysis confirms that the densification and grain growth mechanisms in UHS of AlN are similar to those in conventional techniques, with grain growth being diffusion-controlled via liquid-phase sintering.

Fig. 10 illustrates the Vickers hardness of AlN ceramics sintered under various electric currents and holding times. The Vickers hardness (HV) was calculated using the following equation:

$$HV = \frac{1.854F}{d^2}$$

where d is the diagonal length of the indentation mark, and F is the indentation load. A conversion factor of 0.0098 was applied to convert the hardness values from HV to GPa. Fig. 10a-d show an increasing trend in hardness from 30 to 240 s followed by a decrease at 300 s, regardless

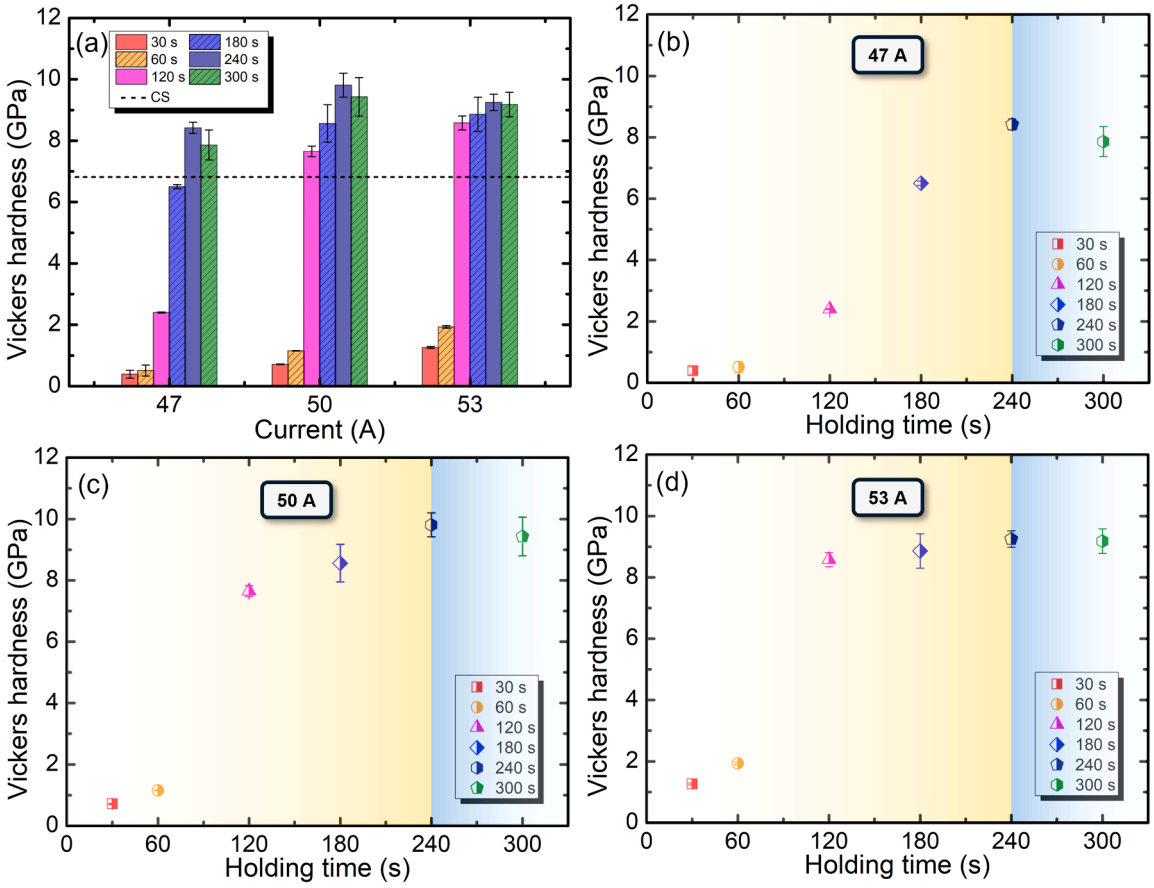

Fig. 10. (a) Vickers hardness of AlN prepared under different electric currents for various holding times. Vickers hardness of AlN prepared under (b) 47 A, (c) 50 A, and (d) 53 A. The Vickers hardness shows an increasing trend up to 240 s, but it decreases at 300 s thereafter.

of the applied currents. Significant increases in hardness are observed between 60 and 120 s. At 50 A, hardness rises from 1.15 ± 0.01 GPa to 7.65 ± 0.17 GPa, and at 53 A, it increases from 1.93 ± 0.04 GPa to 8.58 ± 0.23 GPa. Whereas, the conventionally sintered AlN ceramic exhibited a Vickers hardness of 6.83 ± 0.36 GPa, which is similar to that of the UHS AlN sample processed at 47 A for 3 min. The larger increasing rate for 53 A specimens can be attributed to faster densification due to higher electric current leading to a denser microstructure. However, the decrease in hardness at 300 s for all currents is likely due to several factors. First, the excessive heat during prolonged sintering can cause sublimation of secondary phases, which results in nanopores and lower density, negatively affecting mechanical properties. Secondly, grain growth may contribute to the reduction in hardness of AlN ceramics. According to the Hall-Petch relationship, smaller grains increase hardness by providing more grain boundaries that impede dislocation movement [52,53]. Although dislocation migration is much less active in AlN ceramics due to their covalent nature, the grain boundaries may still play a similar role by impeding the propagation of cracks [54]. Larger grains reduce the number of these boundaries, and thus decrease the hardness as cracks can propagate more easily.

Fig. 11a displays the indentation fracture toughness for specimens with a relative density above 97 %, calculated using the equation by Niihara et al. [55],

$$K_{IF} = 0.0309\left(\frac{E}{H}\right)^{2/5} P c^{-3/2}$$

where K_{IF} is the indentation fracture toughness, E is the elastic modulus, H is the Vickers hardness,

P is the applied load, and c is the crack length from the center of the indentation mark. This method provides accurate indentation toughness values comparable to those obtained via the single edge pre-cracked beam technique for AlN ceramics [56]. The calculated fracture toughness value for the specimen prepared under 47 A for 300 s is 3.09 ± 0.42 MPa·m$^{1/2}$, whereas it is determined to be 2.24 ± 0.27 MPa·m$^{1/2}$ for the specimen processed under 53 A for 300 s. These indicate that larger grains correlate with lower fracture toughness values as shown in Fig. 11a. This trend aligns with other studies showing that non-cubic ceramics exhibit increased toughness with decreasing grain size [54]. Smaller grains create a more uniform microstructure that distributes mechanical stresses more evenly. In contrast, larger grains can introduce non-uniformities and stress concentrations at the boundaries which often become weaker points. This phenomenon is generally influenced by thermal expansion anisotropy (TEA), where differences in thermal expansion coefficients along different crystallographic directions induce internal stress [57]. Numerous grain boundaries combined with small grains act as stress-relief zones that mitigate TEA-induced stresses, and thus enhances toughness. Conversely, fewer boundaries can easily accumulate more stress, and thus promotes microcrack formation and propagation under external load. Additionally, the sublimation of secondary phases due to excessive heat during prolonged sintering can create nanopores at triple junctions and grain boundaries, which act as stress concentration sites for crack nucleation. Fig. 11b-d show the elastic modulus of each specimen, determined from the slope of the unloading curve. In sufficiently dense samples, the elastic modulus values approach the theoretical value of AlN, 308.3 GPa [58]. Whereas the elastic modulus of the conventionally sintered sample was 255.8 ± 7.6 GPa, comparable to the UHS sample processed at 47 A for 3 min, which was 260.5 ± 9.8 GPa.

Among the various conditions tested in this study, the optimal sintering parameters were found to be an electric current of 50 A and a holding time of 240 s. The holding time of 240 s was found to be

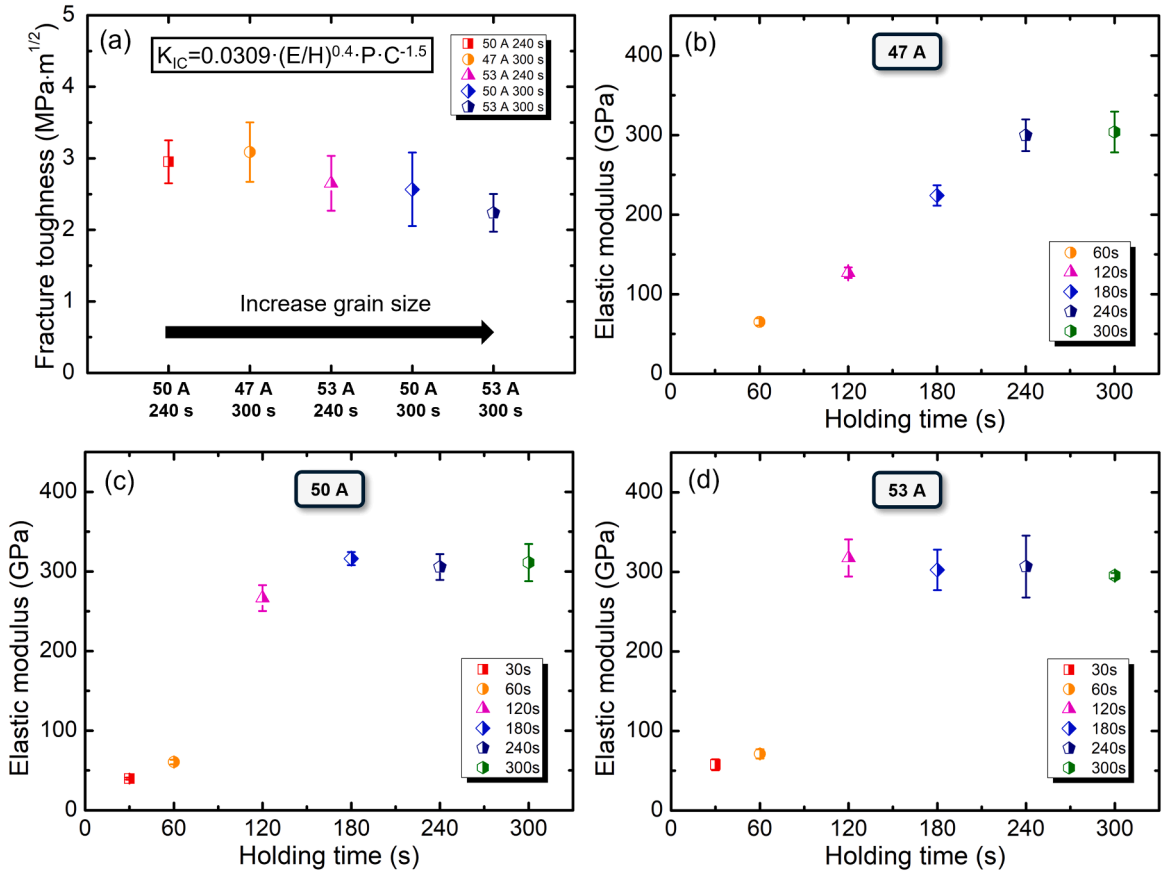

Fig. 11. (a) A plot showing the fracture toughness measured in specimens with a relative density higher than 97 %. Specimens with larger grains tend to exhibit lower fracture toughness. The elastic modulus of the sintered bodies at different electric currents and holding times: (b) 47 A, (c) 50 A, and (d) 53 A.

sufficiently long to achieve high densification, and yet short enough to prevent excessive grain growth. This balance is crucial as longer sintering times can lead to grain coarsening and sublimation of second phases, and thus the degrade mechanical properties. Under these conditions, the AlN ceramic achieved a relative density of 98.8 %, a Vickers hardness of 9.81 ± 0.39 GPa, a fracture toughness of 2.95 ± 0.30 MPa·$m^{1}/^{2}$, and an elastic modulus of 305.71 ± 16.20 GPa. These results demonstrate that UHS can produce high-quality, dense AlN ceramics comparable to those obtained through conventional hot-press sintering method. For comparison, AlN with 5 wt% Y_2O_3 hot-press sintered at 1680°C for 2 h under 20 MPa exhibited a Vickers hardness of 10.42 GPa, a fracture toughness of 3.24 MPa·$m^{1/2}$, and an elastic modulus of 321.5 GPa [54]. The slightly lower mechanical properties of UHS AlN may be attributed to the presence of porosity, which is challenging to eliminate completely without external pressure. Future research should focus on optimizing UHS parameters for AlN ceramics to achieve improved mechanical properties and exploring its application to other challenging non-oxide ceramics.

4. Conclusions

This study demonstrates the applicability and effectiveness of the UHS technique for AlN ceramics with 5 wt% Y_2O_3 as a sintering additive. Various current conditions and sintering times were employed to analyze the relative density, XRD patterns, microstructure, and mechanical properties of each sintered body. Applying electric currents of 47 A, 50 A, and 53 A achieved a relative density above 95 % in just 240 s with corresponding specimen temperatures of 1807.5 °C, 1872.8 °C, and 1935.6 °C, as evaluated by FEM simulations. However, increasing the sintering time to 300 s led to grain growth and the sublimation of second phases formed between Al_2O_3 and Y_2O_3, resulting in a decrease in Vickers hardness. Fracture toughness also decreased with larger grain sizes, consistent with trends in non-cubic ceramics. Overall, the specimen processed under an electric current of 50 A for 240 s exhibited superior performance with a relative density of 98.8 %, a Vickers hardness of 9.81 ± 0.39 GPa, a fracture toughness of 2.95 ± 0.30 MPa·$m^{1/2}$, and an elastic modulus of 305.71 ± 16.20 GPa. These performances are comparable to those of conventionally hot-press sintered AlN suggesting that the UHS method can be effectively applied in the sintering of AlN. These findings shed light on the application of UHS in the manufacturing of advanced non-oxide ceramics, which can provide a more cost-effective and efficient alternative to conventional sintering techniques.

CRediT authorship contribution statement

Minwook Kim: Methodology, Investigation. **Seon-Gyu Kim:** Methodology, Investigation. **Unseo Kim:** Methodology, Investigation. **Sung-Soo Ryu:** Supervision, Funding acquisition. **Yunsang Kwak:** Methodology, Funding acquisition, Conceptualization. **Jaehun Cho:** Writing – review & editing, Writing – original draft, Methodology, Investigation, Funding acquisition, Conceptualization.

Declaration of Competing Interest

The authors declare that they have no known competing financial interests or personal relationships that could have appeared to influence the work reported in this paper.

Acknowledgements

This research was supported by Nano·Material Technology Development Program through the National Research Foundation of Korea (NRF) funded by Ministry of Science and ICT (2022M3H4A3095305). This work was also supported by the National Research Foundation of Korea Grant funded by the Korean Government (NRF-2018R1A6A1A03025761).

Appendix A. Supporting information

Supplementary data associated with this article can be found in the online version at doi:10.1016/j.jeurceramsoc.2024.117025.

References

[1] T. Okada, M. Toriyama, S. Kanzaki, Synthesis of aluminum nitride sintered bodies using the direct nitridation of Al compacts, J. Eur. Ceram. Soc. 20 (2000) 783–787, https://doi.org/10.1016/S0955-2219(99)00204-6.
[2] D. Huang, Z. Liu, J. Harris, X. Diao, G. Liu, High thermal conductive AlN substrate for heat dissipation in high-power LEDs, Ceram. Int 45 (2019) 1412–1415, https://doi.org/10.1016/j.ceramint.2018.09.171.
[3] A.W. Weimer, G.A. Cochran, G.A. Eisman, J.P. Henley, B.D. Hook, L.K. Mills, T. A. Guiton, A.K. Knudsen, N.R. Nicholas, J.E. Volmering, W.G. Moore, Rapid Process for Manufacturing Aluminum Nitride Powder, J. Am. Ceram. Soc. 77 (1994) 3–18, https://doi.org/10.1111/j.1151-2916.1994.tb06951.x.
[4] H. Jiang, X.H. Wang, W. Lei, G.F. Fan, W.Z. Lu, Effects of two-step sintering on thermal and mechanical properties of aluminum nitride ceramics by impedance spectroscopy analysis, J. Eur. Ceram. Soc. 39 (2019) 249–254, https://doi.org/10.1016/j.jeurceramsoc.2018.09.026.
[5] X. Luo, J. Li, B. Zhang, W. Li, H. Zhuang, High thermal conductivity aluminum nitride substrates prepared by aqueous tape casting, J. Am. Ceram. Soc. 89 (2006) 836–841, https://doi.org/10.1111/j.1551-2916.2005.00828.x.
[6] T.B. Troczynski, P.S. Nicholson, Effect of additives on the pressureless sintering of aluminum nitride between 1500° and 1800°C, J. Am. Ceram. Soc. 72 (1989) 1488–1491, https://doi.org/10.1111/j.1151-2916.1989.tb07684.x.
[7] K. Lin, X. Zong, P. Sheng, S. Zhao, Y. Qi, W. Zhang, S. Wu, Effects of SmF3 addition on aluminum nitride ceramics via pressureless sintering, J. Eur. Ceram. Soc. 43 (2023) 6804–6814, https://doi.org/10.1016/j.jeurceramsoc.2023.07.051.
[8] J. Gu, J. Zou, J. Liu, H. Wang, J. Zhang, W. Wang, Z. Fu, Sintering highly dense ultra-high temperature ceramics with suppressed grain growth, J. Eur. Ceram. Soc. 40 (2020) 1086–1092, https://doi.org/10.1016/j.jeurceramsoc.2019.11.056.
[9] Y. Kurokawa, K. Utsumi, H. Takamizawa, Development and microstructural characterization of high-thermal-conductivity aluminum nitride ceramics, J. Am. Ceram. Soc. 71 (1988) 588–594, https://doi.org/10.1111/j.1151-2916.1988.tb05924.x.
[10] D. Huang, Z. Tian, W. Cui, L. Gao, Z. Liu, X. Diao, G. Liu, Effects of Y2O3 and yttrium aluminates as sintering additives on the thermal conductivity of AlN ceramic substrates, Ceram. Int 44 (2018) 20556–20559, https://doi.org/10.1016/j.ceramint.2018.07.178.
[11] H. Sakai, Y. Katsuda, M. Masuda, C. Ihara, T. Kameyama, Effects of adding Y2O3 on the electrical resistivity of aluminum nitride ceramics, J. Ceram. Soc. Jpn 116 (2008) 566–571, https://doi.org/10.2109/jcersj2.116.566.
[12] L. Qiao, H. Zhou, H. Xue, S. Wang, Effect of Y2O3 on low temperature sintering and thermal conductivity of AlN ceramics, J. Eur. Ceram. Soc. 23 (2003) 61–67, https://doi.org/10.1016/S0955-2219(02)00079-1.
[13] H.M. Lee, K. Bharathi, D.K. Kim, Processing and characterization of aluminum nitride ceramics for high thermal conductivity, Adv. Eng. Mater. 16 (2014) 655–669, https://doi.org/10.1002/adem.201400078.
[14] T.B. Jackson, A.V. Virkar, K.L. More, R.B. Dinwiddie, R.A. Cutler, High-Thermal-Conductivity Aluminum Nitride Ceramics: The Effect of Thermodynamic, Kinetic, and Microstructural Factors, J. Am. Ceram. Soc. 80 (1997) 86, https://doi.org/10.1111/j.1151-2916.1997.tb03000.x.
[15] P.S. de Baranda, A.K. Knudsen, E. Ruh, Effect of yttria on the thermal conductivity of aluminum nitride, J. Am. Ceram. Soc. 77 (1994) 1846–1850, https://doi.org/10.1111/j.1151-2916.1994.tb07060.x.
[16] H. Jiang, X.H. Wang, G.F. Fan, W. Lei, M. Fu, X.C. Wang, F. Liang, W.Z. Lu, Effect of hot-pressing sintering on thermal and electrical properties of AlN ceramics with impedance spectroscopy and dielectric relaxations analysis, J. Eur. Ceram. Soc. 39 (2019) 5174–5180, https://doi.org/10.1016/j.jeurceramsoc.2019.08.029.
[17] A. Hafidi, M. Billy, J.P. Lecompte, Influence of microstructural parameters on thermal diffusivity of aluminium nitride-based ceramics, J. Mater. Sci. 27 (1992) 3405–3408, https://doi.org/10.1007/BF01116044.
[18] M. Costantino, C. Firpo, High pressure combustion synthesis of aluminum nitride, J. Mater. Res 6 (1991) 2397–2402, https://doi.org/10.1557/JMR.1991.2397.
[19] L. Qiao, H. Zhou, C. Li, Microstructure and thermal conductivity of spark plasma sintering AlN ceramics, Mater. Sci. Eng. B 99 (2003) 102–105, https://doi.org/10.1016/S0921-5107(02)00429-4.
[20] C. Wang, W. Ping, Q. Bai, H. Cui, R. Hensleigh, R. Wang, A.H. Brozena, Z. Xu, J. Dai, Y. Pei, C. Zheng, G. Pastel, J. Gao, X. Wang, H. Wang, J.-C. Zhao, B. Yang, X. Zheng, J. Luo, Y. Mo, B. Dunn, L. Hu, A general method to synthesize and sinter bulk ceramics in seconds, Science 368 (2020) 521–526, https://doi.org/10.1126/science.aaz7681.
[21] M. Biesuz, S. Grasso, V.M. Sglavo, What's new in ceramics sintering? A short report on the latest trends and future prospects, Curr. Opin. Solid State Mater. Sci. 24 (2020), https://doi.org/10.1016/j.cossms.2020.100868.
[22] M. Kermani, J. Dong, M. Biesuz, Y. Linx, H. Deng, V.M. Sglavo, M.J. Reece, C. Hu, S. Grasso, Ultrafast high-temperature sintering (UHS) of fine grained α-Al2O3, J. Eur. Ceram. Soc. 41 (2021) 6626–6633, https://doi.org/10.1016/j.jeurceramsoc.2021.05.056.

[23] F. Zuo, Q. Wang, Z.Q. Yan, M. Kermani, S. Grasso, G.L. Nie, B.B. Jiang, F.P. He, H. T. Lin, L.G. Wang, Upscaling Ultrafast High-Temperature Sintering (UHS) to consolidate large-sized and complex-shaped ceramics, Scr. Mater. 221 (2022), https://doi.org/10.1016/j.scriptamat.2022.114973.
[24] M.J.H. Reavley, H. Guo, J. Yuan, A.Y.R. Ng, T.Y.K. Ho, H.T. Tan, Z. Du, C.L. Gan, Ultrafast high-temperature sintering of barium titanate ceramics with colossal dielectric constants, J. Eur. Ceram. Soc. 42 (2022) 4934–4943, https://doi.org/10.1016/j.jeurceramsoc.2022.04.056.
[25] J. Wu, Y. Lin, M. Kermani, C. Hu, S. Grasso, Ultra-fast high temperature sintering (UHS) of Li1.5Al0.5Ge1.5P3O12 electrolyte: A rationalization of the heating schedule, Ceram. Int 48 (2022) 6356–6362, https://doi.org/10.1016/j.ceramint.2021.11.178.
[26] F. Ye, F. Meng, T. Luo, H. Qi, Ultrafast high-temperature sintering of (Y0.2Dy0.2Er0.2Tm0.2Yb0.2)4Hf3O12 high-entropy ceramics with defective fluorite structure, J. Eur. Ceram. Soc. 42 (2022) 4686–4691, https://doi.org/10.1016/j.jeurceramsoc.2022.04.023.
[27] R.F. Guo, H.R. Mao, Z.T. Zhao, P. Shen, Ultrafast high-temperature sintering of bulk oxides, Scr. Mater. 193 (2021) 103–107, https://doi.org/10.1016/j.scriptamat.2020.10.045.
[28] J. Wu, Y. Lin, C. Hu, S. Grasso, D. Zhu, J. Li, A. Katz-Demyanitcz, A. Goldstein, Ultra-fast high-temperature sintering of transparent MgAl2O4, Ceram. Int 49 (2023) 19537–19540, https://doi.org/10.1016/j.ceramint.2023.03.018.
[29] Q. Li, H. Du, X. Zhao, F. Zhao, Y. Zhang, X. Hu, X. Du, Densification and microstructure evolution of NaNbO3 ceramic via ultrafast high-temperature sintering, Ceram. Int 50 (2024) 18907–18914, https://doi.org/10.1016/j.ceramint.2024.02.378.
[30] A. Kern, P.J. McGinn, Ultrafast high-temperature sintering of Li7La3Zr1.75Nb0.25Al0.15O12 (LLZO), J. Eur. Ceram. Soc. 42 (2022) 7501–7507, https://doi.org/10.1016/j.jeurceramsoc.2022.08.054.
[31] Y. Lin, N. Luo, E. Quattrocchi, F. Ciucci, J. Wu, M. Kermani, J. Dong, C. Hu, S. Grasso, Ultrafast high-temperature sintering (UHS) of Li1.3Al0.3Ti1.7(PO4)3, Ceram. Int 47 (2021) 21982–21987, https://doi.org/10.1016/j.ceramint.2021.04.216.
[32] A. Alemayehu, M. Biesuz, K.Y. Javan, A. Tkach, P.M. Vilarinho, V.M. Sglavo, V. Tyrpekl, Ultrafast high-temperature sintering of gadolinia-doped ceria, J. Eur. Ceram. Soc. 43 (2023) 4837–4843, https://doi.org/10.1016/j.jeurceramsoc.2023.04.025.
[33] M. Biesuz, T.H. de Beauvoir, E. De Bona, M. Cassetta, C. Manière, V.M. Sglavo, C. Estournès, Ultrafast high-temperature sintering (UHS) vs. conventional sintering of 3YSZ: Microstructure and properties, J. Eur. Ceram. Soc. 44 (2024) 4741–4750, https://doi.org/10.1016/j.jeurceramsoc.2024.01.064.
[34] J. Dong, V. Pouchly, M. Biesuz, V. Tyrpekl, M. Vilémová, M. Kermani, M. Reece, C. Hu, S. Grasso, Thermally-insulated ultra-fast high temperature sintering (UHS) of zirconia: A master sintering curve analysis, Scr. Mater. 203 (2021), https://doi.org/10.1016/j.scriptamat.2021.114076.
[35] J. Wu, M. kermani, D. Zhu, J. Li, Y. Lin, C. Hu, S. Grasso, Carbon free ultra-fast high temperature sintering of translucent zirconia, Scr. Mater. 210 (2022), https://doi.org/10.1016/j.scriptamat.2021.114476.
[36] F. Zuo, Y.N. Deng, Z.X. Liu, Q. Li, S. Grasso, Y.X. Xu, B.B. Jiang, Q.G. Jiang, H. T. Lin, L.G. Wang, Enhancing densification rate and the unusual 4H-SiC polytype stabilization in ultrafast high-temperature sintering of α-SiC, J. Eur. Ceram. Soc. 44 (2024) 610–616, https://doi.org/10.1016/j.jeurceramsoc.2023.09.038.
[37] R.X. Luo, M. Kermani, Z.L. Guo, J. Dong, C.F. Hu, F. Zuo, S. Grasso, B.B. Jiang, G. L. Nie, Z.Q. Yan, Q. Wang, Y.L. Gan, F.P. He, H.T. Lin, Ultrafast high-temperature sintering of silicon nitride: A comparison with the state-of-the-art techniques, J. Eur. Ceram. Soc. 41 (2021) 6338–6345, https://doi.org/10.1016/j.jeurceramsoc.2021.06.021.
[38] B. Zhang, M. Hu, F. Zhong, S. Zhang, Z. Yang, X. Qiu, J. Xu, J. Ou-Yang, Y. Zhang, B. Zhu, X. Yang, S. Chen, Ultrafast high-temperature sintering and densification of ZrC-based ceramics, J. Eur. Ceram. Soc. 44 (2024) 5569–5578, https://doi.org/10.1016/j.jeurceramsoc.2024.03.037.
[39] E. De Bona, C. Manière, V.M. Sglavo, M. Biesuz, Ultrafast high-temperature sintering (UHS) of ZrB2-based materials, J. Eur. Ceram. Soc. 44 (2024) 567–573, https://doi.org/10.1016/j.jeurceramsoc.2023.09.007.
[40] J.S. Thorp, D. Evans, M. Al-Naief, M. Akhtaruzzaman, The dielectric properties of aluminium nitride substrates for microelectronics packaging, J. Mater. Sci. 25 (1990) 4965–4971, https://doi.org/10.1007/BF00580114.
[41] G.A. Slack, T.F. Mcnelly, Growth of High Purity AlN Crystals, J. Cryst. Growth 34 (1976) 263–279, https://doi.org/10.1016/0022-0248(76)90139-1.
[42] M. Yoshida, N. Utsumi, R. Ichiki, J.H. Kong, M. Okumiya, Surface Structure and Emissivity of Aluminum Nitride Films, Adv. Mat. Res 1110 (2015) 163–168, https://doi.org/10.4028/www.scientific.net/amr.1110.163.
[43] J.C. Nipko, C.-K. Loong, Phonon excitations and related thermal properties of aluminum nitride, Phys. Rev. B 57 (1998) 10550–10554, https://doi.org/10.1103/PhysRevB.57.10550.
[44] J. Fukushima, S. Tsubaki, T. Matsuzawa, K. Kashimura, T. Mitani, T. Namioka, S. Fujii, N. Shinohara, H. Takizawa, Y. Wada, Effect of aspect ratio on the permittivity of graphite fiber in microwave heating, Materials 11 (2018), https://doi.org/10.3390/ma11010169.
[45] W. Rheinheimer, X.L. Phuah, L. Porz, M. Scherer, J. Cho, H. Wang, The impact of flash sintering on densification and plasticity of strontium titanate: High heating rates, dislocation nucleation and plastic flow, J. Eur. Ceram. Soc. 43 (2023), https://doi.org/10.1016/j.jeurceramsoc.2023.02.007.
[46] S. Mitra, G. Dutta, I. Dutta, Effect of heat treatment on the microstructure and properties of dense AlN sintered with Y2O3 additions, J. Am. Ceram. Soc. 78 (1995) 2335–2344, https://doi.org/10.1111/j.1151-2916.1995.tb08666.x.
[47] S. -A. Jang, G.M. Choi, Electrical conduction in aluminum nitride, J. Am. Ceram. Soc. 76 (1993) 957–960, https://doi.org/10.1111/j.1151-2916.1993.tb05319.x.
[48] T.-T. Fang, H.P. Iii, Evolution of pore morphology in sintering powder compacts, Ceram. Int 16 (1990) 1–10, https://doi.org/10.1016/0272-8842(90)90056-L.
[49] M. Tajika, H. Matsubara, W. Rafaniello, Experimental and Computational Study of Grain Growth in AlN Based Ceramics, J. Ceram. Soc. Jpn 105 (1997) 928–933, https://doi.org/10.2109/jcersj.105.928.
[50] J. Kanters, U. Eisele, J.R.È. Del, Effect of Initial Grain Size on Sintering Trajectories, Acta Mater. 48 (2000) 1239–1246, https://doi.org/10.1016/S1359-6454(99)00433-4.
[51] G.-F. Xu, T. Olorunyolemi, O.C. Wilson, I.K. Lloyd, Y. Carmel, Microwave sintering of high-density, high thermal conductivity AlN, 2837–2345, J. Mater. Res 17 (2002), https://doi.org/10.1557/JMR.2002.0412.
[52] E. Hall, The Deformation and Ageing of Mild Steel: III Discussion of Results, Phys. Soc. Sect. B 64 (1951) 747–753, https://doi.org/10.1088/0370-1301/64/9/303.
[53] N. Petch, The cleavage strength of polycrystals, J. Iron Steel Inst. 174 (1953) 25–28.
[54] N. Hassan, J. Lee, M. Kim, U. Kim, M. Kim, S. Moon, K. Raju, B. Ahn, I. chul Choi, S. S. Ryu, J. Cho, Enhanced mechanical properties of aluminum nitride-yttria ceramics through grain refinement by pressure assisted two-step sintering, J. Eur. Ceram. Soc. 44 (2024) 831–840, https://doi.org/10.1016/j.jeurceramsoc.2023.09.039.
[55] K. Niihara, R. Morena, D. Hasselman, Evaluation of KIc of brittle solids by the indentation method with low crack-to-indent ratios, J. Mater. Sci. Lett. 1 (1982) 13–16, https://doi.org/10.1007/BF00724706.
[56] H. Miyazaki, Y.I. Yoshizawa, Correlation of the indentation fracture resistance measured using high-resolution optics and the fracture toughness obtained by the single edge-notched beam (SEPB) method for typical structural ceramics with various microstructures, Ceram. Int 42 (2016) 7873–7876, https://doi.org/10.1016/j.ceramint.2016.01.116.
[57] R.W. Rice, Grain size and porosity dependence of ceramic fracture energy and toughness at 22 oC, J. Mater. Sci. 31 (1996) 1969–1983, https://doi.org/10.1007/BF00356616.
[58] D. Gerlich, S.L. Dole, A.A. Slack, Elastic properties of aluminum nitride, J. Phys. Chem. Solids 47 (1986) 437–441, https://doi.org/10.1016/0022-3697(86)90039-9.